Understanding changes in heat waves, droughts, and compound events in Yangtze River Valley and the corresponding atmospheric circulation patterns

Zhonghua Qian[1] · Yingxiao Sun[1] · Qianrong Ma[1] · Yu Gu[2] · Taichen Feng[3,4] · Guolin Feng[1,5]

Abstract

Heat waves, droughts, and compound drought and heat waves (CDHWs) have received extensive attention because of their disastrous impacts on agriculture, ecosystems, human health, and society. Here, we computed the heat wave magnitude index (HWMI), drought magnitude index (DMI), and compound drought and heat wave magnitude index (CDHMI) for Yangtze River Valley (YRV) from July to August during 1961–2022. We compared the large-scale atmospheric circulation characteristics of different extreme events based on these indexes. The results show that the positive center with sink motion in East Asia provides a favorable circulation background for heat wave events. Drought events are mainly affected by the zonal wave train dominated by a significant negative anomaly in Siberia and a high-pressure anomaly upstream, and a anti-cyclonic water vapor with strong divergence over the Yangtze River basin. During CDHW events, both anomalous systems that affect heat waves and droughts appear and strengthen simultaneously. Specifically, in the middle and upper troposphere, the positive height anomaly center in YRV expands abnormally, and the "+−+" wave train over the northern 50° N region of East Asia becomes more obvious. Therefore, the positive anomaly and water vapor anomaly brought by the two circulation patterns at different latitudes are superimposed over the YRV, leading to severe CDHWs. At the same time, the warm positive eddy center and cold negative eddy center in high latitudes exhibit more stable positive pressure features, which are conducive to the persistent development and strengthening of CDHWs. In addition, the anomalous warm sea surface temperature in western Pacific moderating the favorable circulation patterns may also promote the occurrence of CDHWs in the YRV during the same period.

Keywords Heat wave · Drought · Compound drought and heat waves · Yangtze River Valley

✉ Qianrong Ma
maqianron_g@163.com

1 College of Physical Science and Technology, Yangzhou University, Yangzhou 225012, China

2 Jiangsu Yangzhou Meteorological Bureau, Yangzhou 225009, China

3 School of Atmospheric Sciences, Key Laboratory of Tropical Atmosphere-Ocean System, Ministry of Education, Sun Yat-sen University, Zhuhai 519082, China

4 Southern Marine Science and Engineering Guangdong Laboratory, Zhuhai 519082, China

5 Laboratory for Climate Studies, National Climate Center, China Meteorological Administration, Beijing 100081, China

1 Introduction

Both heat waves and droughts have multiple devastating impacts on the ecosystem, agricultural society, and economy and are likely to occur simultaneously (Fischer and Knutti 2013; Leonard et al. 2014; Bastos et al. 2020). The frequency and intensity of heat waves and droughts have increased significantly at the regional and global scales (Seneviratne et al. 2021). Mora et al. (2017) proposed that approximately 30% of the population is exposed to deadly climatic conditions caused by heat waves that have increased in recent years. Meanwhile, droughts are also occurring more frequently with climate warming, leading to an increase in wildfires and a decrease in agriculture production (Field et al. 2012; Alizadeh et al. 2021). Moreover, they will continue to increase with global warming in the future (Gibson et al. 2017; Zscheischler and Lehner 2022). In particular, because

heat waves trigger land surface, boundary layer, and atmospheric warming with strong land–atmosphere feedbacks, the frequency and risks of compound droughts and heat waves (CDHWs) have also increased (Dirmeyer et al. 2013; Hauser et al. 2016; Zscheischler et al. 2018). The combination of extreme events makes climate prediction more difficult (Sedlmeier et al. 2016). Complex and unpredictable impacts and disasters are likely to enhance and threaten ecosystems and human societies (Ciais et al. 2005; Galarneau et al. 2012). Hence, a complete understanding of the characteristics and underlying mechanisms of heat waves, droughts, and CDHWs is of great significance.

Observational and modeling studies have shown that Europe, Russia, the United States, and China have recently experienced many serious heatwaves, droughts, and CDHWs (Sun et al. 2014; Hauser et al. 2016; Ye et al. 2019). Among these, the 2003 and 2010 ''mega-heat waves'' in Europe during summer have attracted global attention (Barriopedro et al. 2011; Bastos et al. 2014). The observed evidence indicates that heat waves in summer modulate atmospheric circulation and soil moisture conditions to enhance the intensity of droughts, thereby increasing evapotranspiration and, in turn, strengthening hot days (Quesada et al. 2012; Xu et al. 2021; Si Gao et al. 2021). Miralles et al. (2019) emphasized that when CDHWs occur, droughts with soil desiccation interact with persistent circulation patterns and entrainment of the boundary layer heat to reinforce the heat wave intensity. Meanwhile, heat waves in the United States respond more strongly to soil moisture and other land surface conditions exacerbated by droughts (Zhou et al. 2019; Lansu et al. 2020). In addition, previous studies have found that heat waves and droughts in China have become more frequent and intense since the late 1990s (Chen and Zhai 2017; Zhu et al. 2020a; Feng et al. 2022). Understanding the mechanisms underlying such extreme events is an urgent necessity owing to their concurrency and profound impacts. Not only land surface processes, but also atmospheric circulation anomalies can trigger heat waves and droughts. For example, anomalous water vapor flux divergence enhanced by the anomalous westward extension of the Western Pacific Subtropical High (WPSH) and an anomalous anticyclone with strong surface net solar radiation led to exceptional heat waves and droughts in the summer of 2003 over eastern China (Zhang et al. 2021). Huang et al. (2016) highlighted the significant influence of atmospheric teleconnections, the Silk Road Pattern (SRP) and East Asia-Pacific/Pacific-Japan (EAP/PJ) teleconnection influenced droughts in East Asia by modulating the position of the WPSH (Chen and Zhai 2015). The EAP/PJ teleconnection has been confirmed as one of the most significant factors in eastern Asian extreme heat waves, which enhances the anticyclone over East Asia via sink motion (Zhu et al. 2020a; Li et al. 2022). Wang et al. (2012) highlighted that the SRP has changed significantly

since the late 1970s because of the weakening of the coupling between the South Asian summer monsoon and mid-latitude circulation, which inhibited moisture transport and caused droughts. Furthermore, anomalous sea surface temperatures (SST) in the western tropical Pacific can affect the spatial features of heat waves in western China by stimulating meridional wave trains (Koenigk et al. 2009; Lin and Li 2018; Zhu et al. 2020b).

In mid-summer (July and August) 2022, unprecedented and enduring heat waves overwhelmed the entire Yangtze River Valley (YRV). He et al. (2023) revealed a seasonal mean daily-maximum temperature anomaly above 3 ℃ along the YRV, breaking the peak of the latest 44 years. Meanwhile, severe droughts occurred concurrently, which led to a serious CDHW and induced wildfire in southwestern China (Sun et al. 2022). The co-occurrence of droughts and heat waves can disproportionately amplify the magnitude of individual events (Mazdiyasni and AghaKouchak 2015), which motivated us to conduct an in-depth study of heat waves, droughts, and CDHWs.

While most studies have focused on heat waves or droughts, little attention has been paid to their comparison on CDHWs (Zhou et al. 2019; Li et al. 2019, 2021; Yang et al. 2020). Owing to global warming, the YRV has experienced frequent CDHWs (Yu and Zhai 2020). The YRV is one of the most important economic development centers in China, which is in the East Asian monsoon region, and features a variety of climatic characteristics (Zhou et al. 2018). Heat waves, droughts, and CDHWs in the YRV vary, and the physical mechanisms underlying these events still need to be investigated. Therefore, this study compared the characteristics of the above-mentioned extreme events and investigated the key atmospheric circulations. The remainder of this paper is organized as follows. First, we introduce the data and methods in Sect. 2 and subsequently illustrate the spatiotemporal characteristics of heat waves, droughts, and CDHWs in July–August in the YRV and the corresponding atmospheric circulations in Sect. 3. Finally, a brief summary and discussion are presented in Sect. 4.

2 Data and methods

2.1 Data

Meteorologically observed daily maximum temperature (T_{max}) and precipitation data from 1961 to 2022 were provided by the National Meteorological Information Centre of the China Meteorological Administration. Among them, observed Tmax and precipitation from 508 meteorological stations in the YRV were collected and subjected to quality-control procedures and homogeneity assessments.
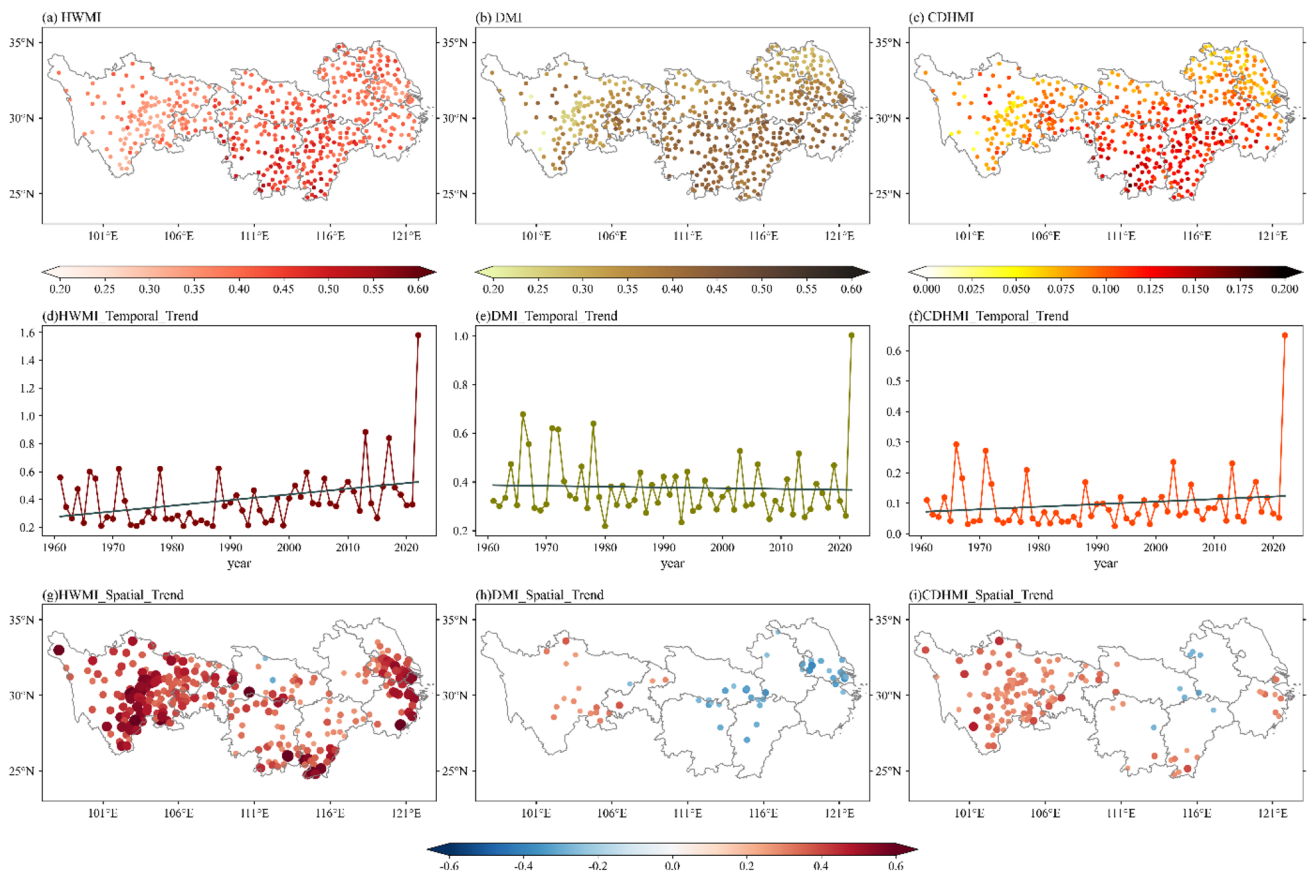
Fig. 1 Spatial distribution of **a** HWMI, **b** DMI, and **c** CDHMI; time series of **d** HWMI, **e** DMI, and **f** CDHMI; and spatial distribution of linear trends for **g** HWMI, **h** DMI, and **i** CDHMI from July to August during 1961–2022, all stations drawn represent significant at α = 0.05 by Student's t test

Monthly atmospheric circulation variables with a resolution of 0.25° × 0.25° were obtained from the ERA5 reanalysis data provided by the the European Center for Medium-Range Weather Forecasting (ECWMF), including potential height, temperature, zonal wind, meridional wind, vertical velocity, and specific humidity with 37 vertical layers during the period 1970–2022 (Hersbach et al. 2020). The land monthly reanalysis data were obtained from the ERA5 monthly land products with horizontal spatial resolution of 0.1°, including potential evaporation, 2 m temperature (T2M), soil moisture (SM) at 0–7 cm, surface net thermal radiation (STR), surface sensible heat flux (SHF), boundary layer height (BLH) during the period 1961–2022 (Muñoz Sabater et al. 2021). The gridded monthly sea surface temperature (SST) data with a resolution of 1.0° were provided by the Met Office Hadley Centre (Rayner 2003). The deviations from the temperature and height zonal means are the eddy height and temperature, respectively (Leung and Zhou 2018).

The vertically integrated water vapor flux and divergence from 1000 to 300 hPa were calculated following Trenberth (1991). Data except SST data are all from July to August, and their climatology and anomalies are calculated based on the period from 1970 to 2022.

2.2 Indexes of heat waves, droughts and CDHWs

The Standardized Precipitation Evapotranspiration Index (SPEI) is defined as monthly precipitation minus evaporation, which reflects meteorological drought severity (Vicente-Serrano et al. 2010a). This drought index was computed using the monthly precipitation stations and potential evaporation (Vicente-Serrano et al. 2010b). To quantify drought magnitude and facilitate the construction of the subsequent compound magnitude index, we applied the drought magnitude index (DMI) based on the monthly SPEI (Zhang et al. 2021). The absolute value of the difference between
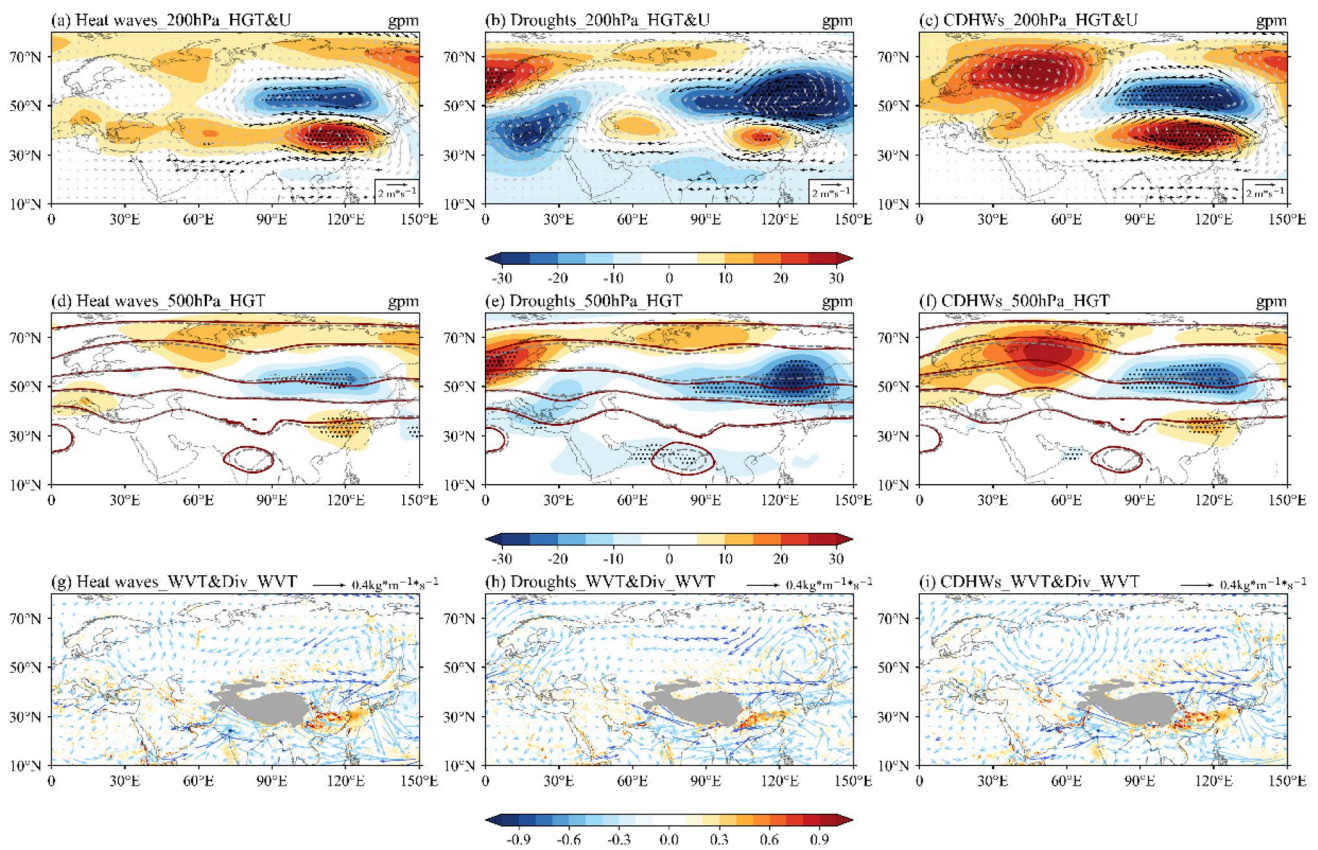
Fig. 2 Composite wind fields anomaly (vectors; unit: $m^{-1}s^{-1}$) and geopotential height at anomaly 200 hPa (shading; unit: gpm) for **a** heat waves, **b** droughts, and **c** CDHWs. Composite geopotential height anomaly (shading; unit: gpm), composite geopotential height (red contour; unit: gpm) and average geopotential height (grey contour; unit: gpm) at 500 hPa for: **d** heat waves, **e** droughts, and **f** CDHWs. Composite anomalous vertical integrated moisture flux (vector; unit: $kg\,m^{-1}\,s^{-1}$) and divergence (shading; unit: $kg\,m^{-1}\,s^{-2}$) for **g** heat waves, **h** droughts, and **i** CDHWs. Dotted areas represent significant at $\alpha = 0.1$ by Student's t test

the SPEI (i.e., SPEI < 10th percentile of SPEI) and threshold (10th percentile of SPEI) was defined to describe the drought magnitude (DI). The DI was then normalized as follows:

$$R_i = 0.9 \times \frac{x_i - x_{min}}{x_{max} - x_{min}} + 0.1$$

where R_i and x_i are the ith normalized result and input data, respectively, and x_{min} and x_{max} are the minimum and maximum values of the input data series, respectively. R|DI| is used to describe the DMI.

In this study, heat waves were defined as T_{max} above the 90th percentile (i.e. each station from July to August during the period 1961–2022) and lasting for at least three days, as calculated by Wang (2017). The final heat wave magnitude index (HWMI) was calculated as:

$$|\Delta T| = |T_{max} - T_{max90th}|$$

$$HWMI = R \sum_{i=1}^{n} |\Delta T_i|$$

where $|\Delta T_i|$ denotes the magnitude of ith heat waves day and $n \geq 3$.

The compound drought and heatwave magnitude index (CDHMI) was established by incorporating the DMI and HWMI. The CDHMI can be calculated as

$$CDHMI = R \sum_{i=1}^{D_n} |\Delta T_i| \times R|DI_n|$$

where D_n is the number of heat waves days for the nth month.

The empirical orthogonal function (EOF) and rotated empirical orthogonal function (REOF) were utilized (Lorenz et al. 1956; Kaiser et al. 1958; Richman et al. 1986). Additionally, we employed multivariate linear regression, linear regression, Pearson correlation analysis, linear trends, and composite methods. Significance was tested using Student's t-test.
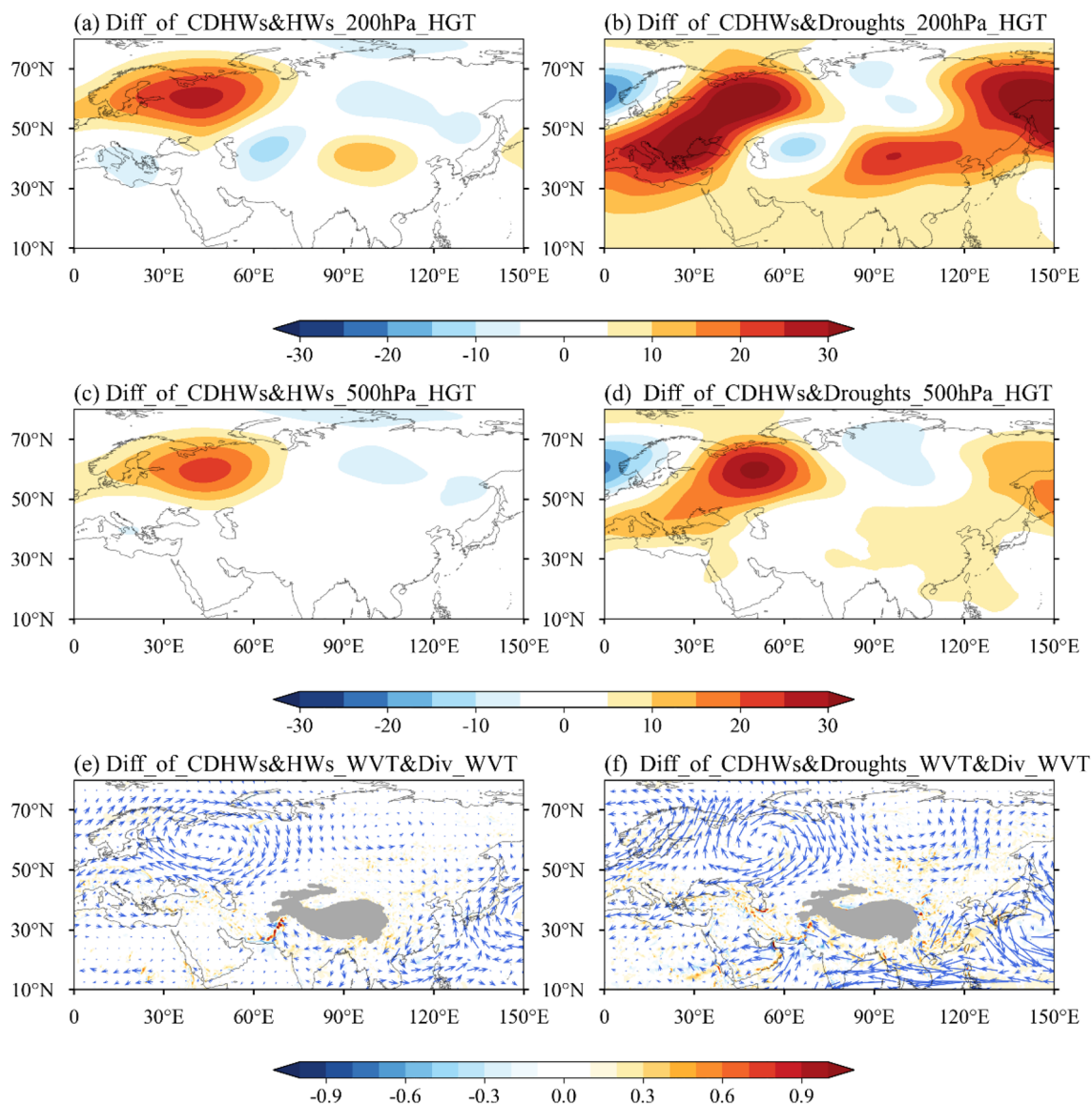
Fig. 3 Composite difference of geopotential height (shading; unit: gpm) at 200 hPa for **a** CDHWs and heat waves and **b** CDHWs and droughts, geopotential height (unit: gpm) for **c** CDHWs and heat waves and **d** CDHWs and droughts, and vertical integrated moisture flux (vector; unit: $kg\,m^{-1}\,s^{-1}$) and its divergence (shading; unit: $kg\,m^{-1}\,s^{-2}$) for **e** CDHWs and heat waves and **f** CDHWs and droughts

2.3 Numerical model simulation

To clarify our conclusions regarding the relationships between SST anomalies and CDHWs in the YRV, the Community Earth System Model 2.0 (CESM2.0) released by the National Center for Atmospheric Research is used for numerical simulation. The Community Atmosphere Model version 5.1 (CAM5.1) of CESM was employed to conduct two experiments. These simulations had a horizontal resolution of 1.9° latitude × 2.5° longitude and 37 vertical layers (Garcia et al. 2007), which included a control and sensitivity experiment.

3 Results

3.1 Spatiotemporal characteristics of heat waves, droughts, and CDHWs in YRV

The spatiotemporal distributions of the HWMI, DMI, and CDHMI in July–August during 1961–2022 in YRV are demonstrated in Fig. 1. Individually, Fig. 1a shows the maximum of HWMI (approximately 0.55) centers in the central of YRV (25° N–32° N, 108° E–118° E). The HWMI in northern Jiangsu and some stations in central Sichuan also had higher values. The DMI showed a maximum (0.50) in the central to southeast region of the study
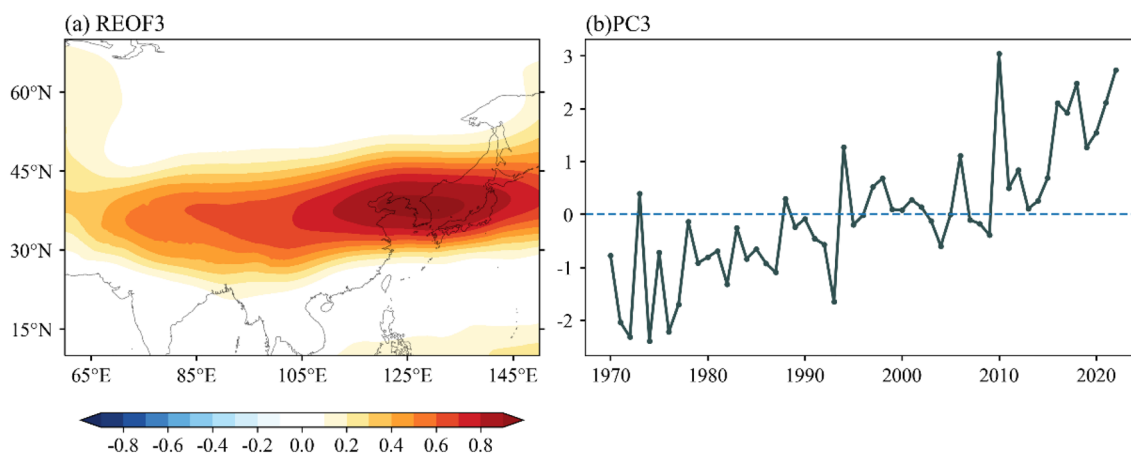
Fig. 4 The geopotential height anomalies at 500 hPa associated with **a** REOF3 and **b** corresponding principal component over the domain 10°–70° N, 60°–150° E during 1970–2022
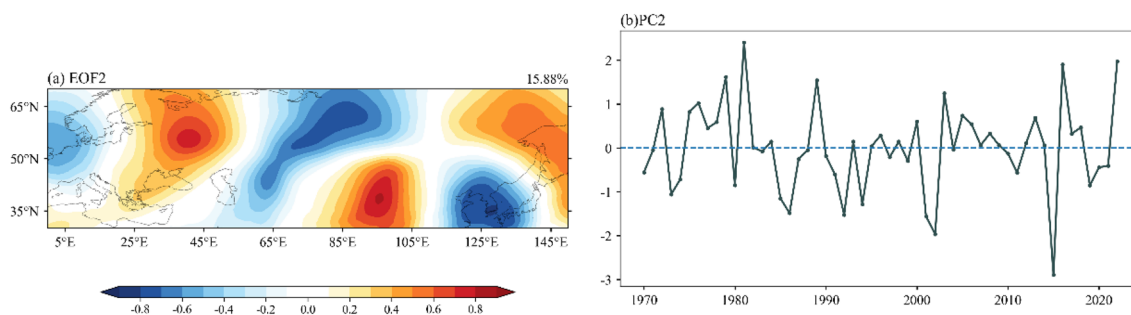

Fig. 5 The meridional wind anomalies at 200 hPa associated with **a** EOF2 and **b** corresponding PC2 over the domain 30°–70° N, 0°–150° E during 1970–2022

area, and larger values were centered in west Sichuan (Fig. 1b). As shown in Fig. 1c, a high CDHMI (0.18) was concentrated in the center of the eastern YRV and northwestern Sichuan. Figure 1d and f present the time series of the three indices that exhibited a peak in 2022. Moreover, the HWMI exhibited a significant upward trend (approximately 0.04) from 1961 to 2022 (exceeding the 95% confidence level), as shown in Fig. 1d. As shown in Fig. 1g, the HWMI showed positive trends at most stations. The DMI exhibited a west–east dipole change, with an increase in the west and decrease in the east (Fig. 1h). The CDHMI illustrates that it is generally increased in the western and eastern YRV, especially in Sichuan Province. In addition, several stations in the north–central YRV decreased (Fig. 1i).

Next, to compare the differences in atmospheric circulation for heat waves, droughts, and compound events, we standardized the index time series and selected the years with standardization passed 0.75 to perform a composite analysis (Figure S1).

3.2 Atmospheric circulation characteristics of heat waves, droughts, and CDHWs

To examine atmospheric circulation associated with heat waves, droughts, and CDHWs, we introduce composite high years for different indices in Fig. 2. A significant dipole pattern over 90° E–120° E and 30° N–60° N at 200 hPa, with a positive center over YRV and negative center over eastern Siberia, is beneficial for heat waves (Fig. 2a). Notably, the positive center extended zonally to the Mediterranean. In Fig. 2d, a similar dipole pattern appears at the same position, which contributes to a strong sink motion over the YRV, triggering heat waves. Notably, water vapor from the western Pacific Ocean may have been transported west by the YRV and converged in northeastern China (Fig. 2g). During drought years, a similar dipole pattern was observed over East Asia; the negative center was more significant and stronger, but the positive center became weaker at 200 hPa in Fig. 2b. Meanwhile, European blocking has significantly strengthened. At 500 hPa, the positive center over the YRV
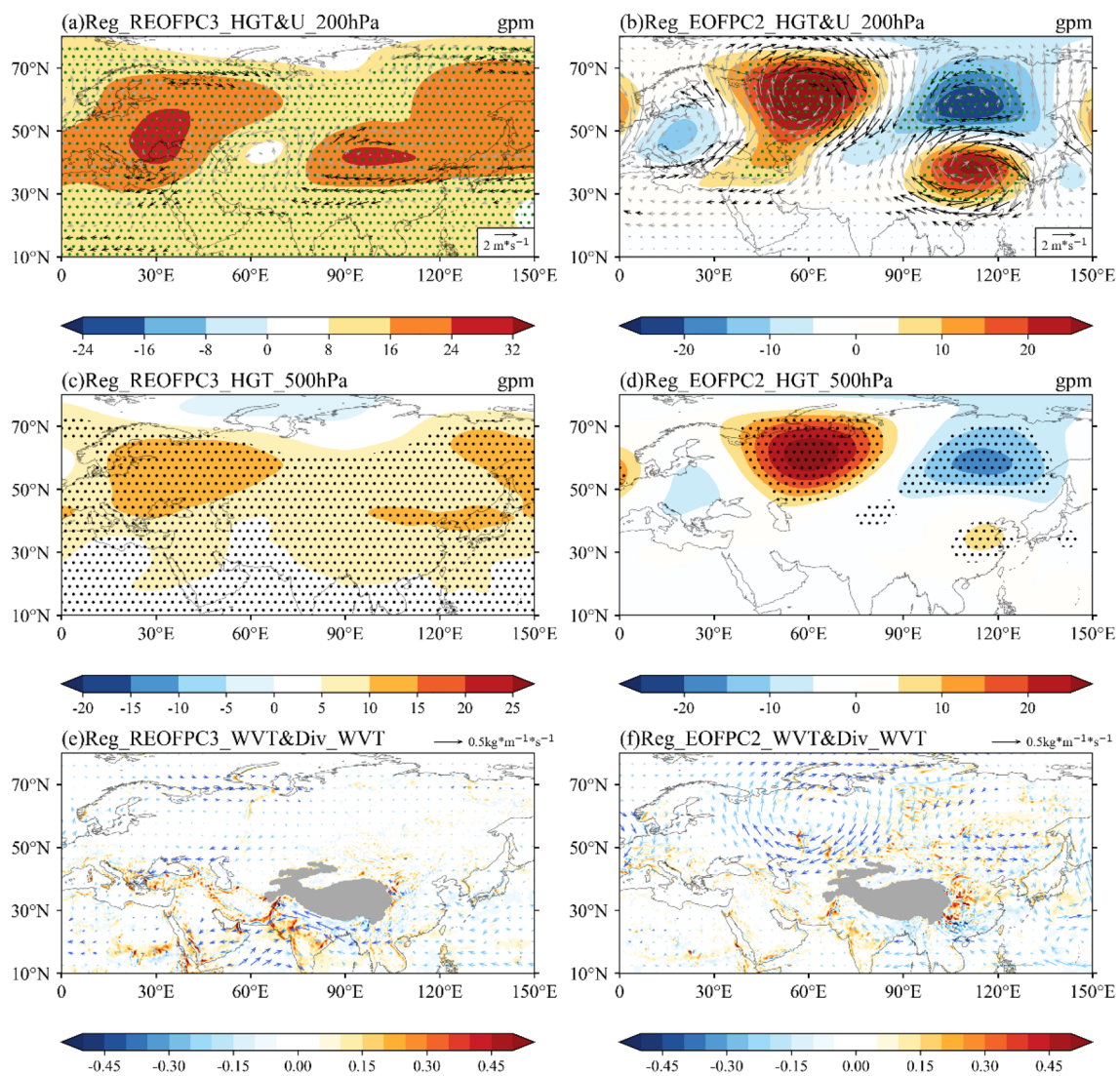
Fig. 6 Regression patterns of the geopotential height (shading; unit: gpm) and wind filed (vector; unit: m s^{-1}) at 200 hPa onto **a** REOF-PC3 and **b** EOF-PC2, geopotential height (unit: gpm) at 500 hPa onto **c** REOF-PC3 and **d** EOF-PC2, and vertical integrated moisture flux (vector; unit: kg m^{-1} s^{-1}) and its divergence (shading; unit: kg m^{-1} s^{-2} onto: **e** REOF-PC3 and **f** EOF-PC2. Regions with dots indicate anomalies that exceed the 95% confidence level

vanished and an anomalous cyclone occurred over the Indian Peninsula (Fig. 2e). Figure 2h shows that water vapor predominantly diverged over the YRV, which substantially suppressed precipitation. Figure 2c displays the anomalous circulation pattern at 200 hPa in the CDHWs, and its meridional characteristic over East Asia resembles Fig. 2a but the wind field is stronger. Moreover, at high latitudes, positive centers over Ural and eastern Siberia and negative centers over Mongolia exhibited similar SRP patterns. At 500 hPa, the circulation pattern largely resembled that at 200 hPa, but the positive center was reduced (Fig. 2f), which provided favorable conditions for CDHWs. As shown in Fig. 2i, the YRV is controlled by an anticyclone located in the middle

of the water vapor divergence and further enhances the CDHWs by increasing droughts.

The differences in the composite circulation patterns of heat waves, droughts, and CDHWs are shown in Fig. 3. Figure 3a first compares heat waves and CDHWs, and the results emphasize that CDHWs years tend to have stronger positive height centers over Europe and northern YRV at 200 hPa. At 500 hPa, European blocking was enhanced when CDHWs occurred (Fig. 3c). In contrast, Fig. 3b shows an obvious wave train over high latitudes, and an anomalous anticyclone controlling the YRV compared with droughts. At 500 hPa, the circulation patterns exhibited structures similar to those at 200 hPa (Fig. 3d). Compared with CDHWs, droughts and heat waves have opposite water vapor transport over YRV.
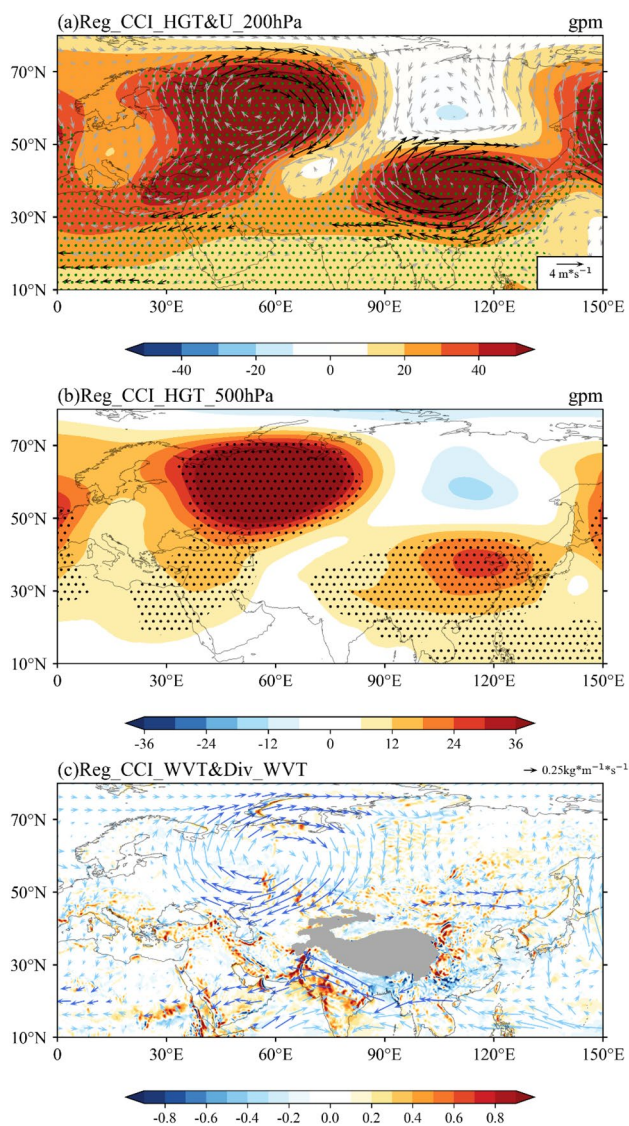
Fig. 7 Regression patterns of **a** geopotential height at 200 hPa (shading; unit: gpm) and winds field (vector; unit: m s^{-1}), **b** 500 hPa height (shading; unit: gpm), and **c** vertical integrated moisture flux (shading; unit: kg m^{-1} s^{-1}) and its divergence (shading; unit: kg m^{-1} s^{-2}) onto CCI. Regions with black dots indicate anomalies that exceed the 95% confidence level

And CDHWs have more significant water vapor divergence in South China (Fig. 3e, f). This is due to the strength and location of the continental high over YRV. Therefore, the combined zonal wave train, European blocking, and anomalous positive center over the YRV contribute to the CDHWs.

3.3 Key circulation mechanisms of CDHWs

Therefore, we focused on the circulation patterns to explore their association with CDHWs. By applying REOF analysis, we acquired the spatiotemporal pattern of circulation over the domain 10°–70° N, 60°–150° E at 500 hPa during

July–August (Figure S2). Figure 4 shows the spatial pattern and corresponding principal component (PC3) of the third REOF mode (REOF3) for geopotential height. The spatial pattern of REOF3 exhibits a zonally distributed positive anomaly centered over the Korean Peninsula, which explained approximately 10.38% of the variance (Fig. 4a). The corresponding PC3 displayed an increasing trend with obvious interannual variations, with the second-highest value in 2022 (Fig. 4b). The correlation between PC3 and HWMI is 0.49 (exceeding the 99% confidence level), whereas the correlation between PC3 and CDHMI is 0.31 (exceeding the 95% confidence level), indicating that the positive anomaly is responsible for heat waves and CDHWs in YRV.

We also examined the second-leading EOF (EOF2) mode of the interannual variability of zonal wind over the domain 30°–70° N, 0°–150° E at 200 hPa, which explained approximately 15.88% of the variance (Fig. 5 and S3). The spatial pattern is characterized by alternating southerly and northerly anomalies along the Eurasian westerly jet at 30° N–70° N, with five well-recognized centers over northern Europe, eastern Europe, central Asia, northwest China, Korean Peninsula, and Okhotsk (Fig. 5a). The corresponding PC2 also exhibited clear interannual variations, with the second-highest value in 2022, as shown in Fig. 5b. PC2 also leads to CDHWs, supported by the significant correlation values (at 95% confidence level) of 0.34 (between PC2 and CDHMI), 0.32 (between PC2 and DMI), and 0.31 (between PC2 and HWMI).

The above circulation modes on CDHWs, circulation anomalies related to the above two modes are displayed in Fig. 6. In the HW mode, the YRV was dominated by positive anomalies, with a significant maximum over East Asia at both 200 and 500 hPa (Fig. 6a, c). These results are consistent with the previous conclusion that anomalous positive centers are favorable for creating more heat waves, as the sink motion occupies the troposphere with persistent westward winds, thereby inhibiting the flow of cold polar winds to the YRV. Regarding the SSRP mode, significant positive centers were individually centered over western Siberia and the YRV, whereas negative centers were over Europe and middle Siberia at 200 hPa (Fig. 6b). Figure 6d shows the equally significant positive centers over western Siberia and the YRV and the negative center over middle Siberia at 500 hPa, whereas the southern positive center is reduced. The anticyclonic water vapor center in the vicinity of the YRV suppresses precipitation because of the relatively large positive values of the diverged water vapor anomalies, which can make the valley prone to drought (Fig. 6f).

To fully elucidate the relationship between circulation patterns and CDHWs, the CDHMI was regressed on PC2 and PC3. We found that the reconstructed CDHMI, i.e., the compound circulation index (CCI) established using
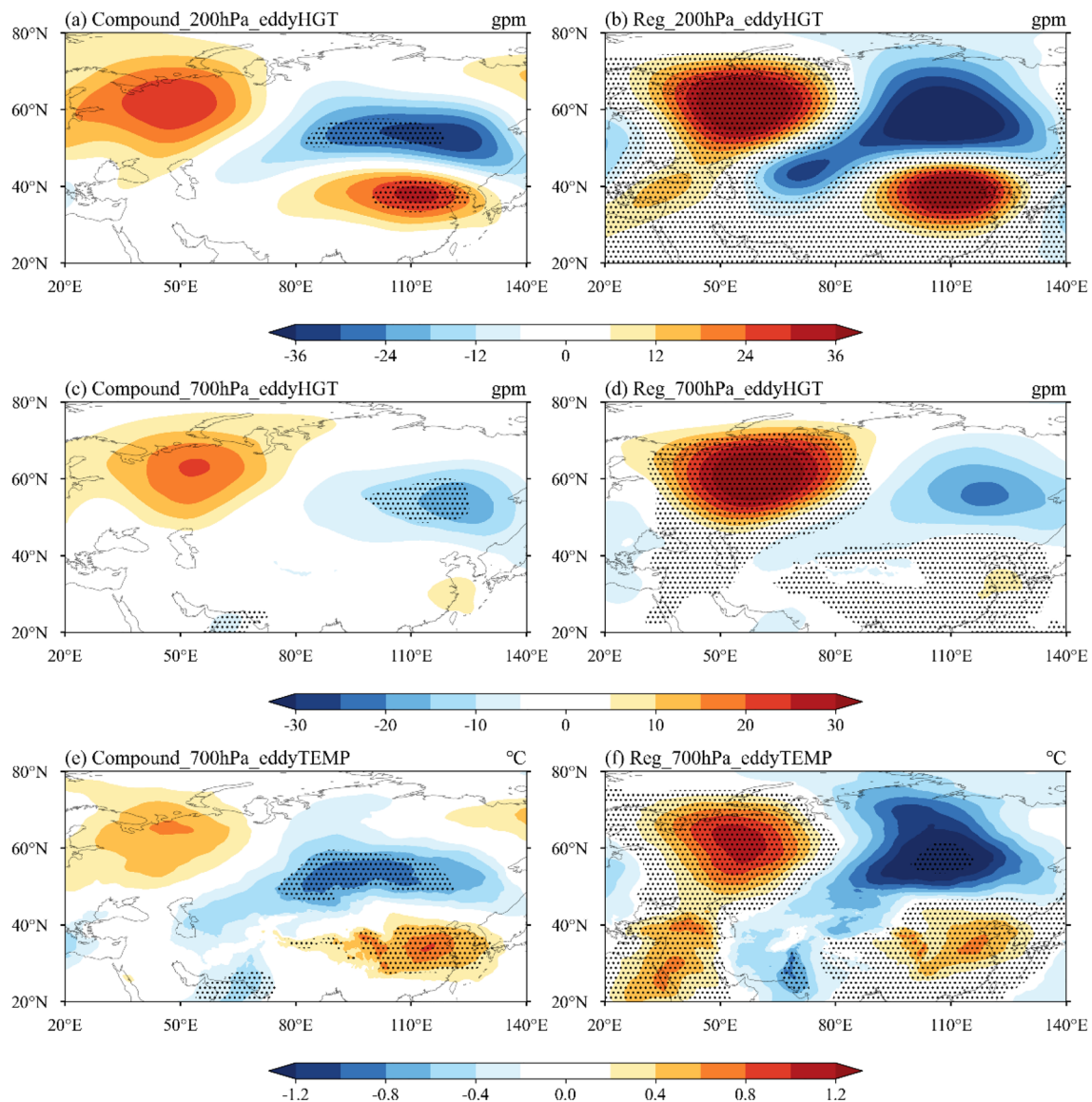
Fig. 8 Composite eddy geopotential height (shading; unit: gpm) for CDHWs at **a** 200 hPa and **c** 700 hPa. Composite eddy temperature (shading; unit: ℃) for CDHWs at **e** 700 hPa. Regression patterns of eddy geopotential height (shading; unit: gpm) at **b** 200 hPa and **d** 700 hPa. Regression patterns of **f** eddy temperature at 700 hPa (shading; unit: ℃) onto CCI. Regions with black dots indicate anomalies that exceed the 95% confidence level

multivariate linear regression (Figure S4), and original CDHMI were significantly correlated (0.46, exceeding the 99% confidence level). The corresponding spatial distribution of the circulation anomalies is presented in Fig. 7. When the values of CCI is higher, two significant positive centers were located over Ural and Southern China at 200 hPa (Fig. 7a). Meanwhile, the entire Eurasian continent south of 45° N was almost shrouded by significant anomalously high pressures. As shown in Fig. 7b, Ural and southern China continued to be covered by significantly positive centers. The YRV is located to the west of the anticyclone and is accompanied by diverged water vapor (Fig. 7c). Thus, the

two circulation patterns combine to form an extremely positive height center over the YRV, making CDHWs prone to be more extreme.

To investigate the persistence of atmospheric circulation associated with CDHWs, we computed the composite and regression eddy parameters, as depicted in Fig. 8. During strong CDHMI years, the troposphere over high-latitude regions exhibited a strikingly lower eddy temperature below the negative eddy center and a higher eddy temperature below the positive eddy center (Fig. 8a, c, e). Similarly, Fig. 8b, d, f show lower and higher eddy temperatures below the negative and positive centers, respectively, indicating
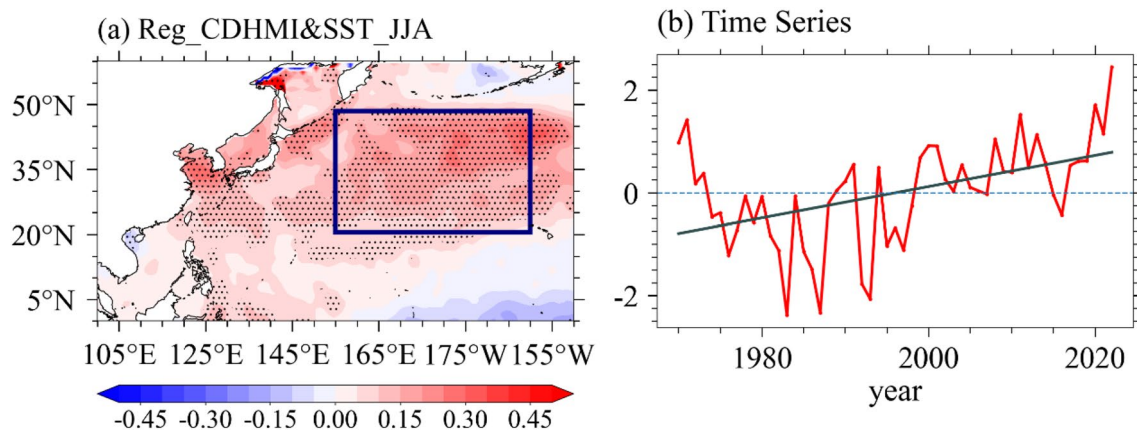
Fig. 9 **a** Regression maps of SST (shading; unit: °C) in JJA with regard to CDHMI. Dotted regions represent regression coefficient significance at the 95% confidence level based on Student's t-test. **b** Standardized time series of the SSTI in JJA from 1970 to 2022

a consistent barotropic pattern. This results in a decrease and increase in height thickness in the lower troposphere, ultimately leading to the endurance of the circulation pattern over high latitudes in the upper troposphere owing to the decrease in thickness in the mid-troposphere.

3.4 Impacts of the Western Pacific SST on circulation

To validate that the anomalous northwestern Pacific positive SST plays a vital role in forcing atmospheric circulation, which is instrumental in CDHWs, Fig. 9 shows the detrended SST in JJA regressed onto the CDHMI from 1970 to 2022. As shown in Fig. 9a, increased CDHMI was accompanied by positive SST anomalies in the western Pacific. Thus, we identified the western Pacific SST index (SSTI) with regional averaged SST in 20° N–48° N, 155–200° E. Figure 9b shows the SSTI from 1970 to 2022, indicating a significant increasing trend (0.03 ℃ a^{-1}, exceeding the 99% confidence level). The correlation coefficient between the CDHMI and SSTI was 0.47 (exceeding the 99% confidence level). Furthermore, the correlation coefficient between the SSTI and CCI was 0.33 (exceeding the 95% confidence level) show that the circulation pattern in CDHWs over the YRV has a very close relationship with increasing northwestern Pacific SST during the period of 1970–2022 (Figure S4).

To confirm that the western Pacific SST anomalies are closely connected to increased extreme circulation. Figure 10 shows the regression maps of SSTI in JJA against the circulation. Figure 10a demonstrates the anomalous anticyclones are centered in Europe (30–60° N, 10–40° E) and almost the whole East Asia at 200 hPa. At 500 hPa, the positive anomalies were like the 200 hPa (Fig. 10b). Furthermore, an anticyclone on the east side of the YRV brought

divergent water vapor, which played a key role in enhancing the CDHWs (Fig. 10c).

To further examine the influence of the western Pacific SST on CDHWs in YRV, two CAM 5.1 numerical experiments were conducted under different SST boundary during JJA, included a control and sensitivity experiments. In the control experiment, the SST are prescribed as boundary conditions in the mode, and the other external variables are fixed. In the sensitive experiment, the SST is increased over the northwestern Pacific in JJA based on the regressed SST, while other months are prescribed by climatological SST. Both experiments were run for 50 years, and the outputs of the last 35 model years were analyzed. Figure 11a shows the responses of the anomalous geopotential height and wind field at 200 hPa. Anomalous anticyclones are centered in Europe (50–60° N, 0–20° E), Kazakhstan, Shandong Peninsula, and east Siberia. Negative center was found in Mongolia. At 500 hPa, except for the positive center in Kazakhstan, the other circulation systems were similar to those at 200 hPa (Fig. 11b). The YRV is located on the southwest side of the anticyclonic water vapor transport, accompanied by roughly divergent water vapor. The above results indicate the influence of increased western Pacific SST on the CDHWs in the YRV using a numerical model, which is mainly consistent with the diagnostic results. In summary, both the diagnosis and numerical simulations showed that the CDHWs were adjusted by increased western Pacific SST anomalies.

3.5 Case of 2022 CDHWs in YRV

The values in 2022 were much higher than those in other years for both CDHMI and CCI. The atmospheric circulation and terrestrial surface variables anomalies were demonstrated in Fig. 12, which can clarify the land-atmosphere
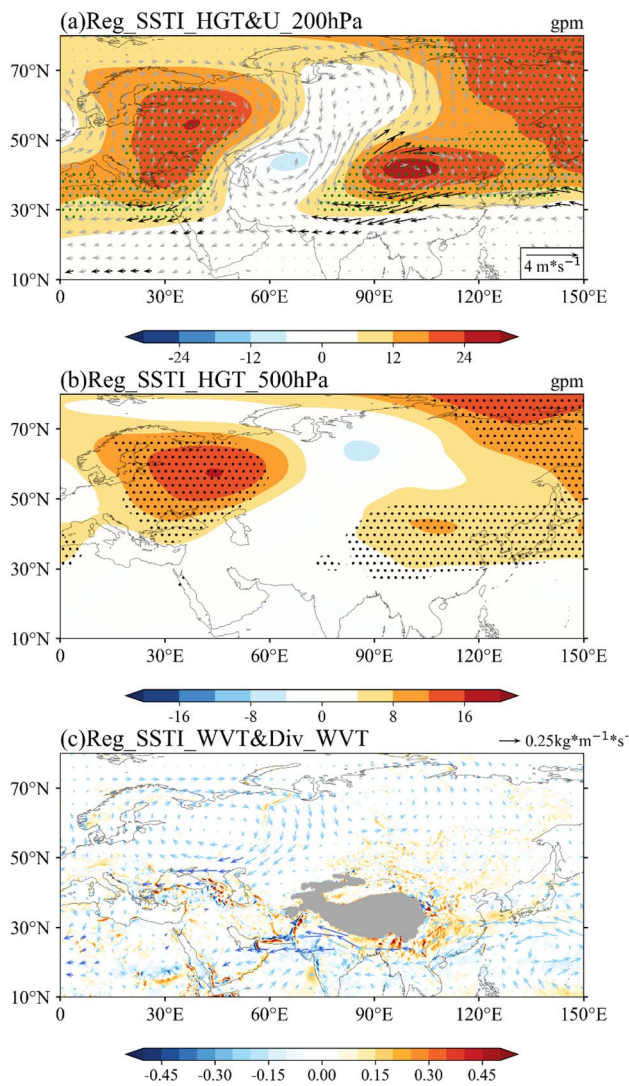
Fig. 10 Regression patterns of **a** geopotential height at 200 hPa (shading; unit: gpm) and winds field (vector; unit: m s^{-1}), **b** 500 hPa height (shading; unit: gpm), and **c** vertical integrated moisture flux (shading; unit: kg m^{-1} s^{-1}) and its divergence (shading; unit: kg m^{-1} s^{-2}) onto SSTI. Regions with black dots indicate anomalies that exceed the 95% confidence level

Fig. 11 Simulation differences between the sensitivity and control experiments (i.e., sensitivity minus control): JA mean climatic **a** 200 hPa wind (vectors; unit: m s^{-1}) and geopotential height (shading; unit: gpm), **b** 500 hPa geopotential height (shading; unit: gpm), and **c** vertical integrated moisture flux (vector; unit: kg m^{-1} s^{-1}) and its divergence (shading; unit: kg m^{-1} s^{-2}) field anomalies forced by SST in the western Pacific for 35 years captured by the CAM5.1 model

interaction. With the positive height and anticyclonic anomalies at 200 and 500 hPa, the whole YRV existed a positive T2M anomaly greater than 1 °C and a negative soil moisture less than -0.05 m^3 m^{-3} (Fig. 12a, c). Meanwhile, the enhanced SHF (decreased latent heat flux by the decreased soil moisture) from land to atmosphere aggravated the magnitude of heat waves. Furthermore, heat fluxes were stored in the boundary layer according to the upward surface long-wave radiation, which was illustrated by the consistent spatial distribution of anomalous positive BLH and upward STR (Fig. 12d). Accordingly, the CDHWs in 2022 was not only influenced by the anomalous atmospheric circulations,

but also further strengthened through the land-atmosphere interaction.

4 Conclusion and discussion

In this study, we analyzed and compared the spatiotemporal characteristics of heat waves, droughts, and CDHWs in the YRV, as well as the differences in circulation patterns, and
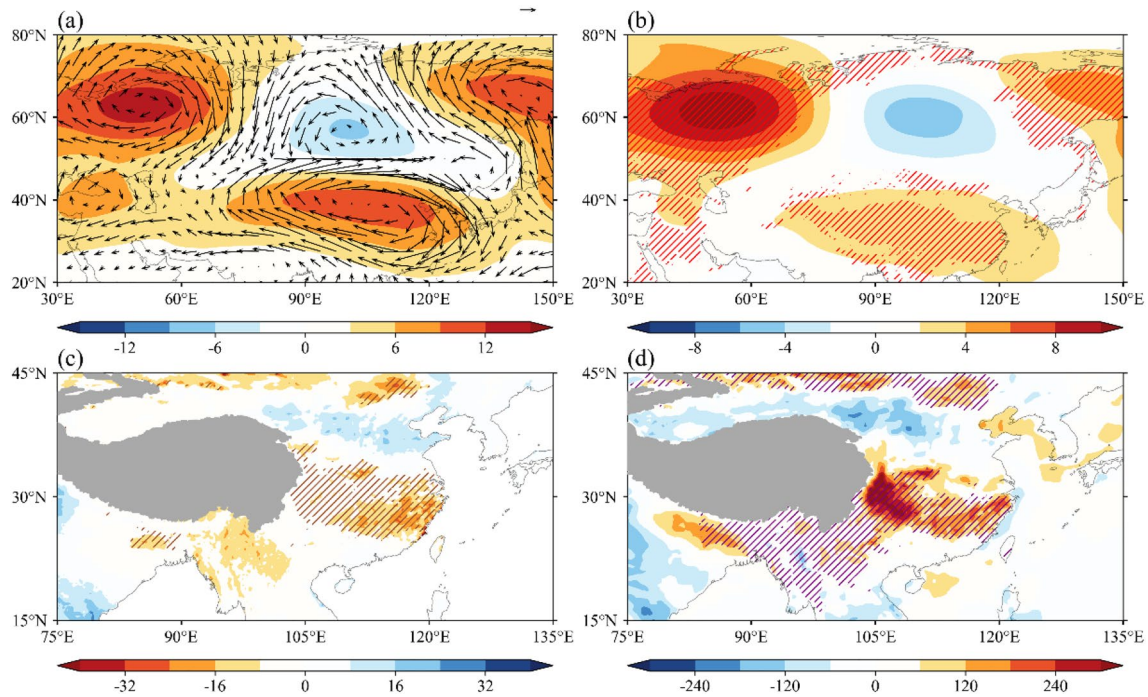
Fig. 12 2022 JA mean anomalies of: **a** 200 hPa wind (vectors; unit: m s^{-1}) and geopotential height (shading; unit: gpm), **b** geopotential height at 500 hPa (shading; unit: gpm) with T2M (hatched line; unit: ℃, only > 1 ℃ is shown), **c** SHF (shading; unit: W m^{-2}) with SM (hatched line; unit: m^3 m^{-3}, only < − 0.05 m^3 m^{-3} is shown), **d** BLH (shading; unit: m) with STR (hatched line; unit: W m^{-2}, only < − 5 W m^{-2} is shown)

further explored the influence of atmospheric circulation and western Pacific SST on CDHWs. We investigated the magnitudes of heat waves, droughts, and CDHWs in the YRV using HWMI, DMI, and CDHMI. We found that heat waves were intensified in northern Jiangsu and the central YRV with a significant increasing trend. The central to southeastern YRV and western Sichuan are prone to droughts, which exhibit a west–east dipole change, with an increase in the west and a decrease in the east. High-magnitude CDHWs were concentrated in the center of the eastern YRV and northwestern Sichuan, whereas only a few stations in the north-central YRV showed significant decreasing trends, which is consistent with previous studies (Ye et al. 2019; Wu et al. 2020). Notably, heatwaves, droughts, and CDHWs all demonstrate their most severe characteristics by 2022.

Large-scale atmospheric circulation can have significant effects on heatwaves, droughts, and CDHWs. The circulation anomalies for each event were different from those of the other two events. For heat waves, the positive center that extends zonally in the YRV results in sink motions that benefit from high temperatures. During droughts, a stable wave train at high latitudes is convenient for the persistence of droughts, and divergent water vapor substantially suppresses precipitation. The combination of the zonal wave train, European blocking, and the anomalous positive center over the YRV ensures the occurrence of CDHWs, while the

land-atmosphere triggered by soil droughts also make the intensity of CDHWs even higher than that of individual extreme events. Specifically, a barotropic structure at high latitudes is conducive to maintaining more stable system development. Meanwhile, the wider range of the positive center, combined with the divergence of water vapor accompanied by the anticyclone, resulted in more severe heat waves and drought features in the CDHWs. Additionally, increasing western Pacific SST can influence the circulation patterns associated with CDHWs. The increasing SST excites positive centers in Europe, Kazakhstan, Shandong Peninsula, and east Siberia, as well as anticyclones accompanied by divergent water vapor via ocean–land interactions, finally leading to CDHWs.

Notably, CCI has shown inconsistencies with CDHMI, such as 2016 (Figure S4). The circulation pattern was like CDHWs' dominating circulations, but only high temperature happened (Ding et al. 2018). The reconstructed CCI only emphasized the influence of the large-scale atmosphere circulations, lacking consideration of the land-atmosphere interaction between compound droughts and heat waves (Zhou and Yuan 2023). Moreover, Yuan et al. (2023) exhibited different droughts events have different time and spital scales and closely associate with evapotranspiration and precipitation changes. Furthermore, previous studies have also suggested the high-latitude zonal wave trains (i.e. Silk Road

Pattern) associated with the subtropical jet likely adjust the CDHWs in China via dynamic and energy processes (White et al. 2017). However, such wave trains variations with climate change are still pending and complex impact on climate extremes remains more investigations (Francis and Vavrus 2012; Wu and Lu 2023). Meanwhile, Mukherjee and Mishra (2021) illustrated more significant CDHWs in China based on CPC temperature, which was caused anthropogenic climate change. Thus, more understanding on how CDHWs changes in a warmer future and related mechanisms are needed.

Declarations

Conflict of interest The authors have no conflict of interest to report.

Ethical approval This study has no human or animal study.

References

Alizadeh MR, Abatzoglou JT, Luce CH, Adamowski JF, Farid A, Sadegh M (2021) Warming enabled upslope advance in western US forest fires. Proc Natl Acad Sci USA 118:e2009717118

Barriopedro D, Fischer EM, Luterbacher J, Luterbacher J, Trigo RM, García-Herrera R (2011) The hot summer of 2010: redrawing the temperature record map of Europe. Science 332:220–224

Bastos A, Gouveia CM, Trigo RM, Running SW (2014) Analysing the spatio-temporal impacts of the 2003 and 2010 extreme heatwaves on plant productivity in Europe. Biogeosciences 11:3421–3435

Bastos A, Ciais P, Friedlingstein P, Sitch S, Pongratz J, Fan L, Wigneron JP, Weber U, Reichstein M, Fu Z, Anthoni P, Arneth A, Haverd V, Jain AK, Joetzjer E, Knauer J, Lienert S, Loughran T, McGuire PC, Tian H, Viovy N, Zaehle S (2020) Direct and seasonal legacy effects of the 2018 heat wave and drought on european ecosystem productivity. Sci Adv 6:eaba2724

Chen Y, Zhai P (2015) Synoptic-scale precursors of the East Asia/Pacific teleconnection pattern responsible for persistent extreme precipitation in the Yangtze River Valley. QJR Meteorol Soc 141:1389–1403

Chen Y, Zhai P (2017) Revisiting summertime hot extremes in China during 1961–2015: overlooked compound extremes and significant changes: overlooked changes of hot extremes. Geophys Res Lett 44:5096–5103

Ciais Ph, Reichstein M, Viovy N, Granier A, Ogée J, Allard V, Aubinet M, Buchmann N, Bernhofer Chr, Carrara A, Chevallier F, De Noblet N, Friend AD, Friedlingstein P, Grünwald T, Heinesch B, Keronen P, Knohl A, Krinner G, Loustau D, Manca G, Matteucci G, Miglietta F, Ourcival JM, Papale D, Pilegaard K, Rambal S, Seufert G, Soussana JF, Sanz MJ, Schulze ED, Vesala T, Valentini R (2005) Europe-wide reduction in primary productivity caused by the heat and drought in 2003. Nature 437:529–533

Ding T, Gao H, Li W (2018) Extreme high-temperature event in southern China in 2016 and the possible role of cross-equatorial flows. Int J Climatol 38:3579–3594

Dirmeyer PA, Jin Y, Singh B, Yan X (2013) Trends in land–atmosphere interactions from CMIP5 simulations. J Hydrometeorol 14:829–849

Feng W, Leung MY-T, Wang D, Zhou W, Zhang OYW (2022) An extreme drought over South China in 2020/21 concurrent with an unprecedented warm Northwest Pacific and La Niña. Adv Atmos Sci 39:1637–1649

Field CB, Barros V, Stocker TF, Qin D, Dokken D, Ebi KL, Mastrandrea MD, Mach KJ, Plattner G-K, Allen SK, Tignor M, Midgley PM (eds) (2012) Managing the risks of extreme events and disasters to advance climate change adaptation: special report of the Intergovernmental Panel on Climate Change, 1st edn. Cambridge University Press, Cambridge

Fischer EM, Knutti R (2013) Robust projections of combined humidity and temperature extremes. Nat Clim Change 3:126–130

Francis JA, Vavrus SJ (2012) Evidence linking Arctic amplification to extreme weather in mid-latitudes. Geophys Res Lett 39:L06801

Galarneau TJ, Hamill TM, Dole RM, Perlwitz J (2012) A multiscale analysis of the extreme weather events over western Russia and Northern Pakistan during July 2010. Mon Weather Rev 140:1639–1664

Garcia RR, Marsh DR, Kinnison DE, Boville BA, Sassi F (2007) Simulation of secular trends in the middle atmosphere, 1950–2003. J Geophys Res 112:D09301

Gibson PB, Pitman AJ, Lorenz R, Perkins-Kirkpatrick SE (2017) The role of circulation and land surface conditions in current and future australian heat waves. J Clim 30:9933–9948

Hauser M, Orth R, Seneviratne SI (2016) Role of soil moisture versus recent climate change for the 2010 heat wave in western Russia. Geophys Res Lett 43:2819–2826

He C, Zhou T, Zhang L, Chen X, Zhang W (2023) Extremely hot East Asia and flooding western South Asia in the summer of 2022 tied to reversed flow over Tibetan Plateau. Clim Dyn 61:2103–2119

Hersbach H, Bell B, Berrisford P, Hirahara S, Horányi A, Muñoz-Sabater J, Nicolas J, Peubey C, Radu R, Schepers D, Simmons A, Soci C, Abdalla S, Abellan X, Balsamo G, Bechtold P, Biavati G, Bidlot J, Bonavita M, De Chiara G, Dahlgren P, Dee D, Diamantakis M, Dragani R, Flemming J, Forbes R, Fuentes M, Geer A, Haimberger L, Healy S, Hogan RJ, Hólm E, Janisková M, Keeley S, Laloyaux P, Lopez P, Lupu C, Radnoti G, de Rosnay P, Rozum I, Vamborg F, Villaume S, Thépaut JN (2020) The ERA5 global reanalysis. QJR Meteorol Soc 146:1999–2049

Huang R, Huangfu J, Liu Y, Du Z, Chen G, Chen W, Lu R (2016) Development from the theory of energy dispersion of Rossby waves to studies on the dynamics of quasi-stationary planetary waves. Chin J Atmos Sci 40(1):3–21

Kaiser HF (1958) The varimax criterion for analytic rotation in factor analysis. Psychometrika 23:187–200

Koenigk T, Mikolajewicz U, Jungclaus JH, Kroll A (2009) Sea ice in the Barents Sea: seasonal to interannual variability and climate feedbacks in a global coupled model. Clim Dyn 32:1119–1138

Lansu EM, Heerwaarden CC, Stegehuis AI, Teuling AJ (2020) Atmospheric aridity and apparent soil moisture drought in European forest during heat waves. Geophys Res Lett 47:e2020GL087091

Leonard M, Westra S, Phatak A, Phatak A, Lambert M, van den Hurk B, Mclnnes K, Risbey J, Schuster S, Jakob D, Stafford-Smith M (2014) A compound event framework for understanding extreme impacts. WIREs Clim Change 5:113–128

Leung MYT, Zhou W (2018) Circumglobal teleconnection and eddy control of variation in summer precipitation over Northwest China. Clim Dyn 51:1351–1362

Li K, Zhang J, Yang K, Wu L (2019) The role of soil moisture feedbacks in future summer temperature change over East Asia. J Geophys Res Atmos 124:12034–12056

Li C, Zwiers F, Zhang X, Li G, Sun Y, Wehner M (2021) Changes in annual extremes of daily temperature and precipitation in CMIP6 models. J Clim 34:3441–3460

Li H, Sun B, Wang H, Zhou B, Duan M (2022) Mechanisms and physical-empirical prediction model of concurrent heatwaves and droughts in July–August over northeastern China. J Hydrol 614:128535

Lin Z-D, Li F (2018) Impact of interannual variations of spring sea ice in the Barents Sea on east asian rainfall in June. Atmos Ocean Sci Lett 11:275–281

Lorenz EN (1956) Empirical orthogonal functions, and statistical weather prediction. Massachusetts Institute of Technology, Department of Meteorology, Cambridge

Mazdiyasni O, AghaKouchak A (2015) Substantial increase in concurrent droughts and heatwaves in the United States. Proc Natl Acad Sci USA 112:11484–11489

Miralles DG, Gentine P, Seneviratne SI, Teuling AJ (2019) Land-atmospheric feedbacks during droughts and heatwaves: state of the science and current challenges: land feedbacks during droughts and heatwaves. Ann NY Acad Sci 1436:19–35

Mora C, Dousset B, Caldwell IR, Powell FE, Geronimo RC, Bielecki CR, Counsell CWW, Dietrich BS, Johnston ET, Louis LV, Lucas MP, McKenzie MM, Shea AG, Tseng H, Giambelluca TW, Leon LR, Hawkins E, Trauernicht C (2017) Global risk of deadly heat. Nat Clim Change 7:501–506

Mukherjee S, Mishra AK (2021) Increase in compound drought and heatwaves in a warming world. Geophys Res Lett 48:e2020GL090617

Muñoz-Sabater J, Dutra E, Agustí-Panareda A, Albergel C, Arduini G, Balsamo G, Boussetta S, Choulga M, Harrigan S, Hersbach H, Martens B, Miralles DG, Piles M, Rodríguez-Fernández NJ, Zsoter E, Buontempo C, Thépaut J-N (2021) ERA5-Land: a state-of-the-art global reanalysis dataset for land applications

Quesada B, Vautard R, Yiou P, Hirschi M, Seneviratne SI (2012) Asymmetric european summer heat predictability from wet and dry southern winters and springs. Nat Clim Change 2:736–741

Rayner NA (2003) Global analyses of sea surface temperature, sea ice, and night marine air temperature since the late nineteenth century. J Geophys Res 108:4407

Richman MB (1986) Rotation of principal components. J Climatol 6:293–335

Sedlmeier K, Mieruch S, Schädler G, Kottmeier C (2016) Compound extremes in a changing climate—a Markov chain approach. Nonlinear Process Geophys 23:375–390

Seneviratne SI, Zhang X, Adnan M, Badi W, Dereczynski C, Di Luca A, Ghosh S, Iskandar I, Kossin J, Lewis S, Otto F, Pinto I, Satoh M, Vicente-Serrano SM, Wehner M, Zhou B (2021) Weather and climate extreme events in a changing climate. Climate change 2021: the physical science basis. Cambridge University Press, Cambridge, pp 1513–1766

Si Gao J, Mao W, Zhang, Zhang F, Shen X (2021) Atmospheric moisture shapes increasing tropical cyclone precipitation in southern China over the past four decades. Environ Res Lett 16:034004. https://doi.org/10.1088/1748-9326/abd78a

Sun Y, Zhang X, Zwiers FW, Song L, Wan H, Hu T, Yin H, Ren G (2014) Rapid increase in the risk of extreme summer heat in Eastern China. Nat Clim Change 4:1082–1085

Sun B, Wang H, Huang Y et al (2022) Characteristics and causes of the hot–dry climate anomalies in China during summer of 2022. Trans Atmos Sci 46:8

Trenberth KE (1991) Climate diagnostics from global analyses: conservation of mass in ECMWF analyses. J Clim 4:707–722

Vicente-Serrano SM, Beguería S, López-Moreno JI (2010a) A Multi-scalar Drought Index sensitive to global warming: the Standardized Precipitation Evapotranspiration Index. J Clim 23:1696–1718

Vicente-Serrano SM, Beguería S, López-Moreno JI, Angulo M, El Kenawy A (2010b) A new global 0.5° gridded dataset (1901–2006) of a Multiscalar Drought Index: comparison with current Drought Index Datasets based on the Palmer Drought Severity Index. J Hydrometeorol 11:1033–1043

Wang H, Wang B, Huang F, Ding Q, Lee J-Y (2012) Interdecadal change of the boreal summer circumglobal teleconnection (1958–2010). Geophys Res Lett 39:L12704

Wang P, Tang J, Sun X, Wang S, Wu J, Dong X, Fang J (2017) Heat waves in China: definitions, leading patterns, and connections to Large-Scale Atmospheric circulation and SSTs: heat waves in China. J Geophys Res Atmos 122:10679–10699.

White RH, Battisti DS, Roe GH (2017) Mongolian mountains matter most: impacts of the latitude and height of asian orography on Pacific wintertime atmospheric circulation. J Clim 30:4065–4082

Wu Y, Lu J (2023) A Quantitative method of detecting transient rossby wave phase speed: no evidence of slowing down with global warming. Adv Atmos Sci 40:251–261

Wu X, Hao Z, Zhang X, Li C, Hao F (2020) Evaluation of severity changes of compound dry and hot events in China based on a multivariate multi-index approach. J Hydrol 583:124580

Xu Z, Chen H, Guo J, Zhang W (2021) Contrasting effect of soil moisture on the daytime boundary layer under different thermo-dynamic conditions in summer over China. Geophys Res Lett 48:e2020GL090989

Yang Y, Zhang M, Li Q, Chen B, Gao Z, Ning G, Liu C, Li Y, Luo M (2020) Modulations of surface thermal environment and agricultural activity on intraseasonal variations of summer diurnal

temperature range in the Yangtze River Delta of China. Sci Total Environ 736:139445

Ye L, Shi K, Xin Z, Wang C, Zhang C (2019) Compound droughts and heat waves in China. Sustainability 11:3270

Yu R, Zhai P (2020) More frequent and widespread persistent compound drought and heat event observed in China. Sci Rep 10:14576

Yuan X, Wang Y, Ji P, Wu P, Sheffield J, Otkin JA (2023) A global transition to flash droughts under climate change. Science 380:187–191

Zhang Y, Mao G, Chen C, Shen L, Xiao B (2021) Population exposure to compound droughts and heatwaves in the observations and ERA5 reanalysis data in the Gan River Basin, China. Land 10:1021

Zhou S, Yuan X (2023) Acceleration of the onset speeds of heat waves over East China by upwind flash droughts. J Geophys Res Atmos 128:e2022JD038072

Zhou D, Bonafoni S, Zhang L, Wang R (2018) Remote sensing of the urban heat island effect in a highly populated urban agglomeration area in East China. Sci Total Environ 628–629:415–429

Zhou S, Williams AP, Berg AM, Cook BI, Zhang Y, Hagemann S, Ruth L, Seneviratne SI, Gentine P (2019) Land–atmosphere feedbacks exacerbate concurrent soil drought and atmospheric aridity. Proc Natl Acad Sci USA 116:18848–18853

Zhu B, Sun B, Wang H (2020a) Dominant modes of interannual variability of extreme high-temperature events in eastern China during summer and associated mechanisms. Int J Climatol 40:841–857

Zhu B, Sun B, Li H, Wang H (2020b) Interdecadal variations in extreme high–temperature events over Southern China in the early 2000s and the influence of the Pacific Decadal Oscillation. Atmosphere 11:829

Zscheischler J, Lehner F (2022) Attributing compound events to anthropogenic climate change. Bull Am Meteorol Soc 103:E936–E953

Zscheischler J, Westra S, van den Hurk BJJM, Seneviratne SI, Ward PJ, Pitman A, AghaKouchak A, Bresch DN, Leonard M, Wahl T, Zhang X (2018) Future climate risk from compound events. Nat Clim Change 8:469–477